Intercalated chalcogenides $Fe_{1/4}TaS_2$ and $Fe_{1/3}TaS_2$ under extreme pressure - temperature conditions

J. L. Musfeldt,[1,2,*] Junjie Yang,[3] R. E. Putnam Jr.,[4] Shengzhi Zhang,[5] J. T. Haraldsen,[4] S. -W. Cheong,[6,7] and Z. Liu[8]

[1]*Department of Chemistry, University of Tennessee, Knoxville, Tennessee 37996, USA*

[2]*Department of Physics and Astronomy, University of Tennessee, Knoxville, Tennessee 37996, USA*

[3]*Department of Physics, New Jersey Institute of Technology, Newark, New Jersey 07102, USA*

[4]*Department of Physics, University of North Florida, Jacksonville, Florida 32224, USA*

[5]*National High Magnetic Field Laboratory, Los Alamos National Laboratory, Los Alamos, New Mexico 87545, USA*

[6]*Department of Physics and Astronomy, Rutgers University, Piscataway, New Jersey 08854 USA*

[7]*Keck Center for Quantum Magnetism, Rutgers University, Piscataway, New Jersey 08854 USA*

[8]*Department of Physics, University of Illinois Chicago, Illinois 60607-7059, USA*

(Dated: October 15, 2025)

Abstract

Intercalation is an important strategy for enhancing functionality in complex chalcogenides. This is because layered materials can be endowed with intriguing properties by filling the van der Waals gap with various ions and molecules, which, in addition to their unique chemistry, break symmetry in new ways. In order to explore the properties of intercalated metal dichalcogenides under extreme pressure-temperature conditions, we combine diamond anvil cell techniques, Raman scattering spectroscopy, magnetic susceptibility, and first-principles calculations to reveal the pressure - temperature phase diagram of $Fe_{1/3}TaS_2$. This system hosts a compression-driven structural phase transition to a polar state as well as remnant charge density wave signatures deriving from the host lamella of the 2H-parent compound. We also explore the role of different A-site patterns and determine that, by comparison, $Fe_{1/4}TaS_2$ is soft and flexible due to the lower metal density inside the van der Waals gap. These findings open the door to entirely new states of matter with exciting property combinations, including metallicity, polarity, chirality, and altermagnetism - depending upon the conditions - that can support a wide range of spintronics and phononics applications.

Keywords: intercalated chalcogenides, natural superlattices, chiral magnets, metallic altermagnets, high pressure Raman scattering, metal monolayer excitations, phase diagrams

* musfeldt@utk.edu

INTRODUCTION

Complex chalcogenides are exceptionally responsive to external stimuli.[1,2] Pressure is particularly well-suited to tuning their properties because, in addition to changing bond lengths and angles, it provides deterministic control of the c/a structural ratio and van der Waals gap.[3,4] Under compression, systems like $CrSiTe_3$, $FePS_3$, $MnPS_3$, and $CrGeTe_3$ host layer sliding, structural phase transitions, insulator-metal transitions, magnetic dimensionality crossovers, piezochromism, the possibility of an orbital-selective Mott transition, and superconductivity.[5] By comparison, intercalated chalcogenides are relatively underexplored.[6–8] Cu_xTiSe_2 (x = 0 - 0.07) has been one of the primary platforms thus far, revealing a competition between the density wave state and superconductivity as well as the development of a full superconducting dome.[9–13] Intercalated van der Waals materials like Fe_xTaS_2 and Cr_xNbS_2 also incorporate atomically-thin networks of metal centers between the transition metal dichalcogenide layers.[14–19] Here, the metal concentration is significantly larger than in the Cu_xTiSe_2 family, and as a result, different patterns are formed within the van der Waals gap depending upon the intercalant concentration (x = 1/4, 1/3).[17,20] The x = 1/3 pattern is especially interesting because it renders the materials non-centrosymmetric and chiral. When incorporated in this manner, metal monolayers support high temperature magnetic ordering,[16,21–27] complex magnetic field - temperature phase diagrams[25,26] novel metallicity distinct from that of the parent compound,[27–31] tunable topological spin textures that interlock with structure,[24,32] asymmetrically-responsive domain walls,[33] skyrmions,[34,35] and superconductivity.[16,36,37] This family of materials may also host altermagnetism.[38–41] Furthermore, intercalated chalcogenides display unique low-frequency excitations that develop systematically in the Raman scattering response with intercalent concentration [Fig. 1].[49,50,53,54] In the x = 1/3 materials like $Cr_{1/3}TaS_2$, these features can be categorized as "in-plane" and "out-of-plane" excitations of the superlattice, although such a simplification neglects interaction with the sulfur centers at the edge of the van der Waals gap.[49] Similar looking low frequency features arise in the x = 1/4 material and in off-stoichiometric compounds,[53] although their assignments are less certain. Non-stoichiometric metal ion concentrations also give rise to charge ordering.[42] At the same time, intercalated chalcogenides like $Fe_{1/3}NbS_2$ are superb platforms for antiferromagnetic spintronic devices.[43–47] Related

systems have been proposed as tunable THz resonators for on-chip[48] and LiDAR applications (night vision for autonomous vehicles)[49,50] as well as topological photonics[51] and even "quantum ink".[52]

In order to explore the properties of intercalated chalcogenides under external stimuli and unravel structure-property relations related to different A-site patterns, we measured the Raman scattering response of $Fe_{1/4}TaS_2$ and $Fe_{1/3}TaS_2$ as a function of pressure and compared our findings to complementary magnetic susceptibility and first-principles calculations. The $x = 1/4$ material is very soft. Compression triggers two critical pressures that separate the $P6_3/mmc$ ground state, a narrow mixed phase region that is present due to the first-order character of the transition, and the high pressure phase. These transitions involve both the embedded Fe monolayer and chalcogenide layers. The overall structural flexibility is likely due to the small size of the metal center and the low-density packing of the metal monolayer inside the van der Waals gap. While the pressure - temperature (P - T) phase diagram of $Fe_{1/3}TaS_2$ also hosts a pressure-driven first-order structural transition, it contains a number of surprises including sensitivity to remnant charge density waves from the 2H-TaS_2 parent compound and a low-pressure edge of the two-phase region that appears to relieve frustration in the iron monolayer and trigger magnetic ordering. Based upon the pattern of peak splittings, a partial group-subgroup analysis, and our complementary first-principles calculations, the high pressure state is probably $P3$. This implies that the $x = 1/3$ compound can host metallicity, chirality, ferroelectricity, and altermagnetism depending upon the conditions. More generally, the tendency for compression to drive chiral, non-centrosymmetric materials into lower symmetry states can be very useful because subgroups of $P6_3/22$ are liable to be piezoelectric and / or ferroelectric - possibly switched by strain. This work opens the door to opportunities for both pressure and strain control along with greater understanding of structure-property trends in this family of intercalated chalcogenides.

RESULTS AND DISCUSSION

Structural phase transitions in $Fe_{1/4}TaS_2$ and $Fe_{1/3}TaS_2$ under pressure

Figures 2 and 3 display the Raman scattering response of $Fe_{1/4}TaS_2$ and $Fe_{1/3}TaS_2$ at room temperature. Both intercalated metal monolayer excitations and the chalcogen layer

phonons are labeled.[49,53,54] The primary differences between these two materials are (i) the density of Fe centers in the metal monolayer ($2a \times 2a$ for $x = 1/4$ and $\sqrt{3}a \times \sqrt{3}a$ for $x = 1/3$) and (ii) the overall crystal symmetry (centrosymmetric $P6_3/mmc$ for $x = 1/4$ vs. chiral + non-centrosymmetric $P6_3/22$ for $x = 1/3$). The chalcogenide layers are identical from a chemical point of view, although the thickness varies slightly [Table I].

Figure 2 summarizes the Raman scattering response of $Fe_{1/4}TaS_2$ under compression. We immediately notice that the excitation near 129 cm^{-1} displays a great deal of symmetry breaking, whereas the feature near 122 cm^{-1} hardens normally under pressure. We assign these structures as superlattice excitations by analogy with the $x = 1/3$ materials. However, alternate assignments are available, including highly collective modes involving Fe, Ta, and S centers [Fig. S4, Supporting Information]. There are noticeable effects in the E_{2g} and A_{1g} symmetry phonons related to the chalcogenide layer as well. Two critical pressures ($P_{C,1} =$ 2.5 GPa and $P_{C,2} = 5.5$ GPa) divide regions of different properties. Based upon the evolution of various phonons under compression [Fig. 2**b-e**], the $P6_3/mmc$ and high-pressure phases are separated by a mixed phase. In other words, the ambient pressure phase is stable up to 2.5 GPa, after which a two-phase region appears, with a high pressure phase of different symmetry emerging above 5.5 GPa. Overall, we find that $Fe_{1/4}TaS_2$ is a very soft material - likely due to the small A-site ion and the low density of metal centers within the van der Waals gap. The Raman scattering response of the $x = 1/4$ material is not reversible upon release of pressure [Fig. S3, Supplementary information].

Figure 3 summarizes the Raman scattering response of $Fe_{1/3}TaS_2$ under compression. The overall character of the symmetry breaking is different from that in the $x = 1/4$ analog, but with equally dramatic effects on the in-plane metal monolayer excitation and chalcogenide layer-derived phonons. To understand the local lattice distortions and how they trigger structural phase transitions, we tracked the frequency shifts and splittings of these features as a function of pressure. The behavior of the superlattice excitation provides a clear indication of the location of the first-order structural phase transition. This feature is sharp and well-defined in the $P6_3/22$ phase, splits into a triplet in the intermediate (mixed phase) region, and exhibits a broad but sharply peaked structure in the high-pressure phase [Fig. 3**b**]. In $Fe_{1/3}TaS_2$ and other $x = 1/3$ materials, superlattice excitations involving metal ion motion are Raman-allowed.[49,50] At the same time, the E_2 and A_1 symmetry intra-layer phonons

harden significantly under pressure and display subtle frequency shifts, splittings, and mode appearances/disappearances under compression [Fig. 3**d,e**]. Based upon these results, we define two critical pressures: $P_{C,1}$ = 3.3 GPa and $P_{C,2}$ = 6 GPa. These critical pressures delineate the lower and upper boundaries of a mixed-phase regime. We therefore find that $Fe_{1/3}TaS_2$ hosts a first-order structural phase transition involving both the Fe monolayer network as well as the chalcogenide layers. As discussed below, the space group of the high-pressure phase is probably $P3$, which is polar.

Comparing $Fe_{1/4}TaS_2$ and $Fe_{1/3}TaS_2$, we see that while the chemistry and size of the A-site ions are identical, the overall density of Fe centers and their pattern within the van der Waals gap are not the same.[17,30] This endows the Fe network in the $x = 1/4$ material with extra space in which to move - which may explain the additional flexibility of the lattice and enhanced symmetry breaking of the metal monolayer excitation under pressure. Two other factors may be at work in the $x = 1/4$ material: (i) a smaller van der Waals gap is likely to support stronger layer interactions with metal centers, and (ii) the thicker chalcogenide layer is expected to be more flexible and prone to distortion [Table I].

Developing the temperature - pressure phase diagram of $Fe_{1/3}TaS_2$

In order to explore the properties of intercalated chalcogenides more deeply, we measured the Raman scattering response of $Fe_{1/3}TaS_2$ as a function of pressure at a series of fixed temperatures using a custom-built cryostat that enables us to change pressure *in situ*. We employed the protocol developed at room temperature for relating changes in the vibrational response to the critical pressures, and we used these findings to define phase boundaries and develop the pressure-temperature (P - T) phase diagram. We brought these results together with the measurements of the ferromagnetic ordering temperature under pressure [Fig. S6, Supplementary information] to more fully illustrate the relationship between charge, structure, and magnetism in this system.

Figure 4 displays the P - T phase diagram of $Fe_{1/3}TaS_2$. Focusing first on the high temperature portion of the phase diagram, we find that the stability of the $P6_3/22$ ground state diminishes with decreasing temperature. In fact, extrapolation of $P_{C,1}$ yields approximately 35 K - the exact magnetic ordering temperature for this system.[17] This suggests that the

symmetry breaking that takes place due to the formation of the two-phase regime may be sufficient to relieve magnetic frustration in the metal monolayer and allow the Fe moments to order. We find that $P_{C,2}$ decreases in a similar manner, so that the size of the two-phase regime remains relatively constant with decreasing temperature. This type of hysteretic mixed phase region is a well-known signature of a first-order transition.[59]

The character of the P - T phase diagram changes dramatically below 100 K. As shown in Fig. 4, both $P_{C,1}$ and $P_{C,2}$ turn upward near 100 K, reach a maximum near 50 K, and then drop slightly toward the base temperature. But why does $Fe_{1/3}TaS_2$ host enhanced interaction between the charge, spin, and structural channels in this part of the phase diagram? It turns out that this is a very active area of the phase diagram for 2H-TaS_2 as well, and while $Fe_{1/3}TaS_2$ is a unique material in its own right, it retains some of the tendencies that make the parent compound so exciting. For instance, 100 K is an energy scale that corresponds to the development of charge density waves in 2H-TaS_2.[55,56] Clearly, the fundamental excitations of the lattice in the intercalated material are sensitive to a remnant of this effect - even though the significant density of states at the Fermi level in the $x = 1/3$ material[30] might be expected to eliminate charge density wave nesting. 2H-TaS_2 also hosts an incommensurate charge density wave transition at 85 K and superconductivity below 1 K. Both evolve across this pressure range.[57,58]

In addition to revealing phase competition, we can use the P - T phase diagram to analyze the thermodynamics of $Fe_{1/3}TaS_2$. Examination of the structural phase boundary lines defined by our Raman scattering measurements reveals that $\partial P/\partial T$ is positive above 100 K. Since the Helmholtz energy requires -$\partial P/\partial T)_V$ = -$\partial S/\partial V_T$, this implies that $\partial S/\partial V$ should be positive. Volume diminishes under compression, so the change in entropy must be negative as well. That $Fe_{1/3}TaS_2$ hosts a metal monolayer whose entropy is probably decreasing as the chalcogenide layers come closer together may be responsible for such an observation. The opposite argument applies to the structural transitions at low temperature as well as the development of long-range magnetic order under compression because the phase boundary lines bend the other way. As shown in Fig. 4 and in more detail in the Supplementary information, the ferromagnetic ordering temperature in $Fe_{1/3}TaS_2$ decreases with pressure. A similar trend is observed in $Cr_{1/3}TaS_2$ and $Cr_{1/3}NbS_2$.[18,60,61]

Symmetry of the high-pressure phase

In addition to developing the phase diagram, we can use these spectra to partially unravel the symmetry of the high pressure state in $Fe_{1/3}TaS_2$. This approach works because irreducible representations of distinct crystal phases exhibit the full crystal symmetry.[63] A full solution is obviously impossible because the sample is metallic[28–30] and, as a result, the infrared modes are screened by the Drude oscillator.[30,62] This means that we are unable to uncover direct evidence for loss of the inversion center. We can still identify a few candidate space groups in the absence of infrared phonon trends, but can not conclusively reveal the full space group without the help of additional techniques and/or theory, which we present below. We begin with the $P6_3/22$ space group (number 182) and recall that it is chiral and non-centrosymmetric.[17] A group-subgroup analysis using the Bilbao server[64,65] reveals that there are four different subgroups immediately available to this system: $P312$, $P321$, $P6_3$, and $C222_1$. Of these, only $P6_3$ is polar. There are several suitable subgroups below this level, all of which are polar. They include $P3$, $C2$, $C2$ in a different setting, and $P2_1$. $P1$ resides at the bottom of the "symmetry tree" [Fig. S5, Supplemental information]. Based upon symmetry breaking in the metal monolayer and chalcogen layer under pressure [Fig. 3], we hypothesize that the high pressure phase in $Fe_{1/3}TaS_2$ hosts a space group that is two levels below $P6_3/22$. Theory is consistent with this supposition and suggests a $P3$ space group. The key point at this time is that the $P3$ space group as well as the other choices appear to be both chiral and polar.[66] We therefore see that $Fe_{1/3}TaS_2$ has the potential to host metallicity, chirality, ferroelectricity, and magnetism (depending upon the conditions).

Density functional theory supports this picture of a pressure-driven structural phase transition in the $x = 1/3$ material. In addition to a decrease in the van der Waals gap and concomitant drop in the magnetic moment [Fig. 5**a,b**], our calculations reveal that $Fe_{1/3}TaS_2$ undergoes a $P6_3/22 \rightarrow P3$ transition. As mentioned above, the $P3$ space group is polar and chiral. Similar effects are observed in the $x = 1/4$ system, although here, we predict that the high pressure space group of $Fe_{1/4}TaS_2$ is Cm. The latter is also polar but not chiral.[66] This description of symmetry breaking in the iron intercalated chalcogenides is quite different from the behavior of $Cr_{1/3}TaS_2$, which is surprisingly robust under compression and does not display substantial structural distortions in this pressure range.[50]

We can use these results to develop a schematic pressure - composition (P - x) phase diagram for the Fe_xTaS_2 series of materials [Fig. 5**c**]. The key point is that the low and high pressure phases are separated by a mixed phase region in both compounds, and that the high pressure states appear to host polar space groups. It remains to determine whether the $x = 1/4$ and $1/3$ materials are ferroelectric (switchable) or pyroelectric (not switchable) under these conditions.

Developing structure-property relationships in the Fe_xTaS_2 family of materials

Thus far, we combined Raman scattering spectroscopy, magnetic susceptibility, and first-principles calculations to explore the properties of intercalated chalcogenides under pressure and uncover the role of different A-site patterns in the Fe_xTaS_2 family of materials. Much of our work focuses on revealing the pressure - temperature phase diagram of $Fe_{1/3}TaS_2$. The phase diagram of this chiral magnet is extremely interesting because, in addition to evidence for a first-order structural transition under compression, it is sensitive to remnant effects deriving from the 2H-TaS_2 parent compound (like the charge density wave transition at 100 K) which change the overall shape of the phase boundaries. We speculate that two effects work together to suppress the magnetic ordering transition[67] in this system: (i) the structural phase transitions at $P_{C,1}$ and $P_{C,2}$ that involve the fundamental excitations of the lattice and (ii) the charge density wave transition with associated electron-phonon coupling that ought to be fragile but somehow survives in remnant form near 100 K. A partial group-subgroup analysis, along with our calculations, suggests that the high pressure phase of $Fe_{1/3}TaS_2$ may be polar. This demonstrates that the $x = 1/3$ material has the potential to host a number of simultaneous properties, including metallicity, ferroelectricity, chirality, and magnetism. Given the number of unique metal sites and magnetic symmetry of this system, it is possible that $Fe_{1/3}TaS_2$ is a metallic altermagnet. By comparison, the $x = 1/4$ analog is significantly softer, with low frequency Fe-containing excitations that display strong spin-phonon coupling across T_C[49] as well as extensive symmetry breaking under pressure that we attribute to the enhanced chalcogen layer thickness, overall lower metal density, and more modest size of the van der Waals gap compared with that of the A site ion. That said, the character of the low frequency excitations in $Fe_{1/4}TaS_2$ deserves additional scrutiny, and unraveling the

pressure - temperature phase diagram is anticipated to reveal even stronger magnetoelastic interactions although without the chirality that typifies the $x = 1/3$ material. Whether these high pressure phases and their associated properties can also be accessed under strain is a topic for future work.

METHODS

Crystal growth and loading the diamond anvil cell: High-quality single crystals of several different intercalated transition metal dichalcogenides were grown via flux techniques as described previously.[17] We chose $Fe_{1/4}TaS_2$ and $Fe_{1/3}TaS_2$ in order to explore structure-property relations in this family of materials. Small, well-shaped pieces of each crystal were selected and loaded into suitably-chosen diamond anvil cells with either KBr or Ar as the pressure medium to ensure quasi-hydrostatic pressure conditions [Fig. 1**d** and Fig. S1, Supplementary information]. The Ar load was especially important below 125 K and needed to locate the pressure-induced transitions in a reproducible manner. An annealed ruby ball was included to determine pressure via fluorescence.[68,69] Two different symmetric diamond anvil cells were used in this work. Both employed synthetic high-temperature-high pressure type II as low-fluorescence diamonds with either 500 or 600 μm culets. We used large diamond culets to make it easier to change pressure at low temperatures. These measurements also employed 50 μm thick pre-indented stainless steel gaskets with 200 μm diameter holes.

Raman scattering spectroscopy under pressure: We performed Raman scattering measurements (10 - 600 cm^{-1}) using a 532 nm (green) laser with 3.5 mW power, a triple monochrometer, and a liquid nitrogen-cooled CCD detector. Scans were between 30 and 60 seconds, averaged 5 or 10 times, depending on the need. Pressure was increased between 0 and 11 GPa - first at room temperature and then at several lower temperatures (250, 200, 150, 125, 100, 80 K, and so on down to 12 K) using a custom-built cryostat that accommodates the diamond anvil cell and supports *in-situ* compression measurements. For the low-temperature experiments, one ruby ball was positioned inside the sample chamber while another was placed on the diamond back plate as a temperature reference.[68,69] We monitored the shape of the ruby fluorescence spectrum at each measurement temperature to

ensure that the sample remained in a quasi-hydrostatic environment Fig. S2, Supplementary information]. We used both liquid nitrogen and helium for cryogenic cooling. Although an open-flow system, this cryostat is limited to operating above approximately 12 K, even with helium, to control the step size during isothermal compression of the diamond anvil cell. Our protocol for determining the position of each phase transition was developed at room temperature and then extended to low temperatures. The spectral signatures of each phase are discussed in detail in the text. Finally, we point out that many of the phase transitions are reversible upon release of pressure. In some cases, recompression of the sample and subsequent release give identical results, so crystal quality can remain high. In other cases, the pressure-induced transitions are not entirely reversible, likely due to disorder. Comparisons of the pristine and pressure-cycled materials are provided in Fig. S3 of the Supplementary information.

Magnetic property measurements: Magnetic moment as a function of temperature was measured under four different pressures using a vibrating sample magnetometer in a 0.2 T magnetic field. A self-clamped CuBe piston-cylinder cell was employed, with Daphne 7373 oil as the pressure-transmitting medium. Inside the pressure cell, a $Fe_{1/3}TaS_2$ single crystal was aligned with its *c*-axis parallel to the applied magnetic field. The pressures were determined by measuring the superconducting transition temperature of a small tin manometer placed in the cell alongside the $Fe_{1/3}TaS_2$ crystal. Additional information can be found in the Supplementary Information.

First-principles calculations: Density functional calculations were performed using QuantumATK within a spin-polarized generalized gradient approximation (SGGA), a Perdew, Burke, and Ernzerhof (PBE) exchange-correlation, and a PseudoDojo pseudopotential.[70–73] The calculations were run with a Grimme DFT-D3 van der Waals correction[74]. Structures were geometry optimized to a maximum force of 0.01 Å/eV and applied constrained and unconstrained isotropic pressure from 0 to 9 GPa. The calculations employed a k-point sampling of 6x6x3 with a tolerance of 10^{-5} Hartrees. The system was assumed to have a ferrromagnetic configuration determined in Fan *et al.*[30], which is the ground state for the system. To reduce computational parameters, no Hubbard U nor spin-orbit coupling was used in the calculations. Additionally, we provide a detailed discussion of the low-frequency phonons in the Fe_xTaS_2 system is given in the Supplementary information.

DATA AVAILABILITY

Data are available from the corresponding author upon reasonable request.

SUPPORTING INFORMATION

Supplementary information is available regarding the sample inside the diamond anvil cell and ruby fluorescence under pressure as well as a comparison of pristine vs. released spectra. We also provide magnetic properties data and some detail on the low frequency phonons of these intercalated materials (PDF).

ACKNOWLEDGEMENTS

JLM thanks Physical Behavior of Materials, Basic Energy Sciences, U.S. Department of Energy (Contract number DE-SC0023144) for support of this work. SWC is funded by a W. M. Keck foundation grant to the Keck Center for Quantum Magnetism at Rutgers University. JY acknowledges support by DOE under Grant No. DOE: DE-SC0021188. JTH and REP acknowledge funding from the Institute for Materials Science at Los Alamos National Laboratory. Work at the National Synchrotron Light Source II at Brookhaven National Laboratory is funded by the Department of Energy (DE-AC98-06CH10886). Use of the 22-IR-1 beamline is supported by the National Science Foundation - Earth Sciences via Synchrotron Earth and Environmental Science (SEES) EAR-22232736 and Chicago/DOE Alliance Center (CDAC) DE-NA0003975. We thank J. Analytis, S. Fan, Y. Gu, I. Mazin, and J. G. Park for useful conversations.

AUTHOR CONTRIBUTIONS

JLM designed the study. JY and SWC grew the crystals. JLM and ZL performed the high pressure spectroscopic measurements. JLM analyzed the spectral data. JY and SZ measured magnetic properties under pressure. REP performed complementary first-principles calculations under the guidance of JTH. JLM, JY, and JTH designed the figures and wrote the manuscript. All authors read and commented on the text.

COMPETING INTERESTS

The authors declare no competing interests.

---

[1] Miro, P., Audiffred, M., and Heine, T. An atlas of two-dimensional materials. *Chem. Soc. Rev.* **43**, 6537-6554 (2014).

[2] Park, J. -G. *et al.*, 2D van der Waals magnets: from fundamental physics to applications, arXiv: 2505.02355v1.

[3] Grochala, W., Hoffmann, R., Feng, J., and Ashcroft, N. W. The chemical imagination at work in very tight places. *Angew. Chem. Int. Ed.* **46** 3620-3642 (2007).

[4] Pei, S., Wang, Z., and Xia, J. High pressure studies of 2D materials and heterostructures: A review. *Materials Design* **213**, 110363 (2022).

[5] Matsuoka, T. *et al.*, $M\mathrm{P}X_3$ van der Waals magnets under pressure (M = Mn, Ni, V, Fe, Co, Cd; X = S, Se). *Frontiers in Materials* **11**, 1362744 (2024).

[6] Wang, Z., Li, R., Su, C., and Loh, K. P. Intercalated phases of transition metal dichalcogenides. *Smart Mat.* **1**, e1013, (2020).

[7] Rajapakse, M. *et al.* Intercalation as a versatile tool for fabrication, property tuning, and phase transitions in 2D materials. npj 2D Mater. Applic. **5**, 30 (2021).

[8] Tezze, D. *et al.* Tuning the magnetic properties of $NiPS_3$ through organic-ion intercalation. *Nanoscale* **14**, 1165-1173 (2022).

[9] Snow, C. S. *et al.* Quantum melting of the charge-density-wave in 1T-$TiSe_2$. *Phys. Rev. Lett.* **91**, 136402 (2003).

[10] Morosan, E. *et al.* Superconductivity in Cu_xTiSe_2. *Nature Phys.* **2**, 544-550 (2006).

[11] Barath, H. *et al.* Quantum and classical mode softening near the charge density wave - superconductor transition in Cu_xTiSe_2. *Phys. Rev. Lett.* **100**, 106402 (2008).

[12] Kusmartseva, A. F. *et al.* Pressure induced superconductivity in pristine 1T-$TiSe_2$. Phys. Rev. Lett. **103**, 236401 (2009).

[13] Yan, S. *et al.*, Influence of domain walls in the incommensurate charge density wave state of Cu intercalated 1T-$TiSe_2$. *Phys. Rev. Lett.* **118**, 106405 (2017).

[14] Liu, Y. *et al.* Electrical and thermal transport in van der Waals magnets 2H-MTaS$_2$ (M = Mn, Co). *Physical Review Research* **4**, 013048 (2022).

[15] Du, K. *et al.* Strain-control of cycloidal spin order in a metallic van der Waals magnet. Adv. Mater. 2303750 (2023).

[16] Morosan, E. *et al.* Sharp switching of the magnetization in $Fe_{1/4}TaS_2$. *Phys. Rev. B.* **75**, 104401 (2007).

[17] Horibe, Y. *et al.* Color theorems, chiral domain topology, and magnetic properties of Fe_xTaS_2. *J. Am. Chem. Soc.* **136**, 8368-8373 (2014).

[18] Mito, M. *et al.* Investigation of structural changes in chiral magnet $Cr_{1/3}NbS_2$ under application of pressure. *J. Appl. Phys.* **117**, 183904 (2015).

[19] Liu, H. *et al.* Elastically induced magnetization at ultrafast time scales in a chiral helimagnet. *Phys. Rev. B* **106**, 035103 (2022).

[20] Craig, I. M. *et al.* Modeling the superlattice phase diagram of the transition metal intercalation in bilayer 2h-TaS$_2$. *J. Amer. Chem. Soc.* **147**, 13629 -13641 (2025).

[21] Togawa Y. *et al.* Chiral magnetic soliton lattice on a chiral helimagnet. *Phys. Rev. Lett.* **108**, 107202 (2012).

[22] Tenasini, G. *et al.*, Giant anomalous Hall effect in quasi-two-dimensional layered antiferromagnet $Co_{1/3}NbS_2$. *Phys. Rev. Res.* **2**, 023051 (2000).

[23] Sirica, N. *et al.* The nature of ferromagnetism in the chiral helimagnet $Cr_{1/3}NbS_2$. *Commun. Phys.* **3**, 65 (2020).

[24] Du, K. *et al.* Topological spin-structure couplings in layered chiralmagnet $Cr_{1/3}TaS_2$: The discovery of spiral magnetic superstructure. Proc. Nat. Acad. Sci. **118**, e2023337118 (2021).

[25] Xie, L. S. *et al.* Structure and magnetism of iron- and chromium-intercalated niobium and tantalum disulfides. *J. Am. Chem. Soc.* **144**, 9525–9542 (2022).

[26] Husremovic, S. *et. al.*, Hard ferromagnetism down to the thinnest limit of iron-intercalated tantalum disulfide. *J. Am. Chem. Soc.* **144**, 12167-12176 (2022).

[27] An, Y. *et. al.*, Bulk properties of the chiral metallic triangular antiferromagnets $Ni_{1/3}NbS_2$ and $Ni_{1/3}TaS_2$. *Physical Review B* **108**, 054418 (2023).

[28] Hu, W. Z. *et. al.* Optical study of the charge-density-wave mechanism in 2H-TaS$_2$ and Na_xTaS_2. *Phys. Rev. B* **76**, 045103 (2007).

[29] Mankovsky, S. *et. al.* Electronic, magnetic, and transport properties of Fe-intercalated 2H-TaS_2 studied by means of the KKR-CPA method. *Phys. Rev. B* **92**, 144413 (2015).

[30] Fan, S. *et. al.* Electronic chirality in the metallic ferromagnet $Fe_{1/3}TaS_2$. *Phys. Rev. B.* **96**, 205119 (2017).

[31] Xie, L. S. *et. al.*, Comparative electronic structures of the chiral helimagnets $Cr_{1/3}NbS_2$ and $Cr_{1/3}TaS_2$. *Chemistry of Materials* **35**, 7239-7251 (2023).

[32] Ghosh, S. *et al.* Raman spectroscoic evidence for linearly dispersed nodes and magnetic ordering in the topological semimetal $V_{1/3}NbS_2$. arXiv:2504:04590v1.

[33] Karna, S. K. *et al.* Annihilation and control of chiral domain walls with magnetic field. *Nano Letters* **21**, 1205-1212 (2021).

[34] Park, P. *et al.*, Tetrahedral triple-Q magnetic ordering and large spontaneous Hall conductivity in the metallic triangular antiferromagnet $Co_{1/3}TaS_2$. *Nat Commun* **14**, 8346 (2023).

[35] Park, P. *et al.*, Composition dependence of bulk properties in the Co-intercalated transition metal dichalcogenide $Co_{1/3}TaS_2$. *Phys. Rev. B* **109**, L060403 (2024).

[36] Li, L. J. *et. al.* Fe-doping-induced superconductivity in the charge-density-wave system 1T-TaS_2. *Euro. Phys. Lett.* **97**, 67005 (2012).

[37] Zhang, Y. *et al.* Kramers nodal lines in intercalated TaS_2 superconductors. *Nature Commun.* **16**, 4984 (2025).

[38] Candelora, C. *et al.* Discovery of intertwined spin and charge density waves in a layered altermagnet. arXiv:2503.03716

[39] Ray, M. K. *et al.* Zero-field Hall effect emerging from a non-Fermi liquid in a collinear antiferromagnet $V_{1/3}NbS_2$. *Nature Commun.* **16**, 3532 (2025).

[40] Sprague, M. *et al.*, Observation of altermagnetic spin-splitting in an intercalated transition metal dichalcogenide. arXiv: 2508.12985v1.

[41] Meng, Z. *et al.*, Spontaneous topological Hall effect in intercalated $Co_{1/3}TaS_2$ nanoflakes with non-co-planar antiferromagnetic order, *Advanced Functional Materials*, 2502016 (2025).

[42] Wu, S. *et al.* Discovery of charge order in the transition metal dichalcogenide Fe_2NbS_2. *Phys. Rev. Lett.* **131**, 186701 (2023).

[43] Nair, N. L *et al.*, Electrical switching in a magnetically intercalated transition metal dichalcogenide. *Nature Mater.* **19**, 153-157 (2020).

[44] Little, A. *et al.* Three-state nematicity in the triangular lattice antiferromagnet $Fe_{1/3}NbS_2$. *Nat. Mater.* **19**, 1062-1067 (2020).

[45] Yang, S. H. Spintronics on chiral objects. *Appl. Phys. Lett.* **116**, 120502 (2020).

[46] Amin, O. J., Edmonds, K. W., and Wadley, P. Electrical control of antiferromagnets for the next generation of computing technology. *Appl. Phys. Lett.* **117**, 010501 (2020).

[47] Mi, M. *et al.* Two-dimensional magnetic materials for spintronic devices. *Materials Today Nano*, **24**, 100408 (2023).

[48] Yang, Y. *et al.* Terahertz topological photonics for on-chip communication. *Nat. Photonics* **14**, 446-451 (2020).

[49] Fan, S. *et al.* Fundamental excitations of intercalated metal monolayers in transition metal dichalcogenides. *Nano Lett.* **21**, 99 (2021).

[50] Musfeldt, J. L. *et al.* Giant tunability of superlattice excitations in chiral $Cr_{1/3}TaS_2$. *npj Quantum Materials* **10**, 27 (2025).

[51] Choi, C. W. Three practical uses for topological photonics. *IEEE Spectrum* **57**, 9-10, (2020).

[52] Baraghani, S. *et al.* Charge-density-wave thin-film devices printed with chemically exfoliated 1T-TaS_2 ink. *ACS Nano* **16**, 6325–6333 (2022).

[53] Erodici, M. P. *et al.* Bridging structure, magnetism, and disorder in iron-intercalated niobium diselenide, Fe_xNbSe_2, below $x = 0.25$. *The Journal of Physical Chemistry C* **127**, 9787-9795 (2023).

[54] Lawrence, E. A. *et al.*, Fe site order and magnetic properties of $Fe_{1/4}NbS_2$. *Inorganic Chemistry* **62**, 18179–18188 (2023).

[55] Yokota, K., Kurata, G., Matsui, T., and Fukuyama, H. Superconductivity in the quasi-two-dimentional conductor 2H-$TaSe_2$. *Physica B* **284-288**, 551-552 (2000).

[56] Joshi, J. *et al.* Short-range charge density wave order in 2H-TaS_2. *Phys. Rev. B* **99**, 245144 (2019).

[57] Grasset, R. *et al.* Pressure-induced collapse of the charge density wave and Higgs mode visibility in 2H-TaS_2. *Physical Review Letters* **122**, 127001 (2019).

[58] Freitas, D. C. *et al.* Strong enhancement of superconductivity at high pressures within the charge-density-wave states of 2H-TaS_2 and 2H-$TaSe_2$. *Physical Review B* **93**, 184512 (2016).

[59] Musfeldt, J. L., Mandrus, D. G., and Liu, Z. Insulator-metal transition in $CrSiTe_3$ triggered by structural distortion under pressure. *npj 2D Materials and Applications* **7**, 28 (2023).

[60] Kanomata, T. *et al.* Magnetovolume effect of ternary compound $Cr_{1/3}TaS_2$. *Cryst. Res. Technol.* **31**, 655 (1996).

[61] M. Mito *et al.* Nonlinear magnetic susceptibility measurements at GPa-level pressures. *J. Phys.: Conf. Ser* **215**, 012182 (2010).

[62] Harms, N. C. *et al.* Symmetry progression and possible polar metallicity in $NiPS_3$ under pressure, npj 2D Materials and Applications **6**, 40 (2022).

[63] J. L. Musfeldt *et al.* Structural phase purification of bulk HfO2:Y through pressure cycling. *Proceedings of the National Academy of Sciences* **121**, e2312571121 (2024).

[64] Kroumova, E. *et al.* Bilbao crystallographic server: useful databases and tools for phase transition studies. Phase Transit. **76**, 155–170 (2003).

[65] Aroyo, M. I. *et al.* Bilbao crystallographic server. ii. representations of crystallographic point groups and space groups. *Acta Crystallogr.* **A62**, 115–128 (2006).

[66] Litvin, D. B. Ferroelectric space groups. *Acta Cryst.* **A42**, 44-47 (1986).

[67] Li, N. *et al.* Abnormal hot carrier decay via spin–phonon coupling in intercalated van der Waals ferromagnetic $Fe_{1/3}TaS_2$. *Nano Lett.* **22**, 3849–3855 (2022).

[68] Mao, H. K., Bell, P. M., Shaner, J. W., and Steinberg, D. J. Specific volume measurements of Cu, Mo, Pd, and Ag and calibration of the ruby R_1 fluorescence pressure gauge from 0.06 to 1 Mbar. *J. Appl. Phys.* **49** 3276-3283 (1976).

[69] Mao, H. K., Xu, J., and Bell, P. M. Calibration of the ruby pressure gauge to 800 kbar under quasi-hydrostatic conditions. *J. Geophys. Res.* **91**, 4673-4676 (1986).

[70] QuantumATK version R-2020.09

[71] Smidstrup, S. *et al.* QuantumATK: An integrated platform of electronic and atomic-scale modelling tools. *J. Phys: Condens. Matter* **32**, 015901 (2020).

[72] Perdew, J. P. *et al.* Generalized gradient approximation made simple. *Phys. Rev. Lett.* **778**, 3865 (1996).

[73] Van Setten, M. J. *et al.* The PseudoDojo: Training and grading a 85 element optimized norm-conserving pseudopotential table. *Comput. Phys. Commun.* **226**, 39 (2018).

[74] Caldeweyher, E. *et al.* Extension of the D3 dispersion coefficient model. *J. Chem. Phys.* **147**, 034112 (2017).

FIGURES

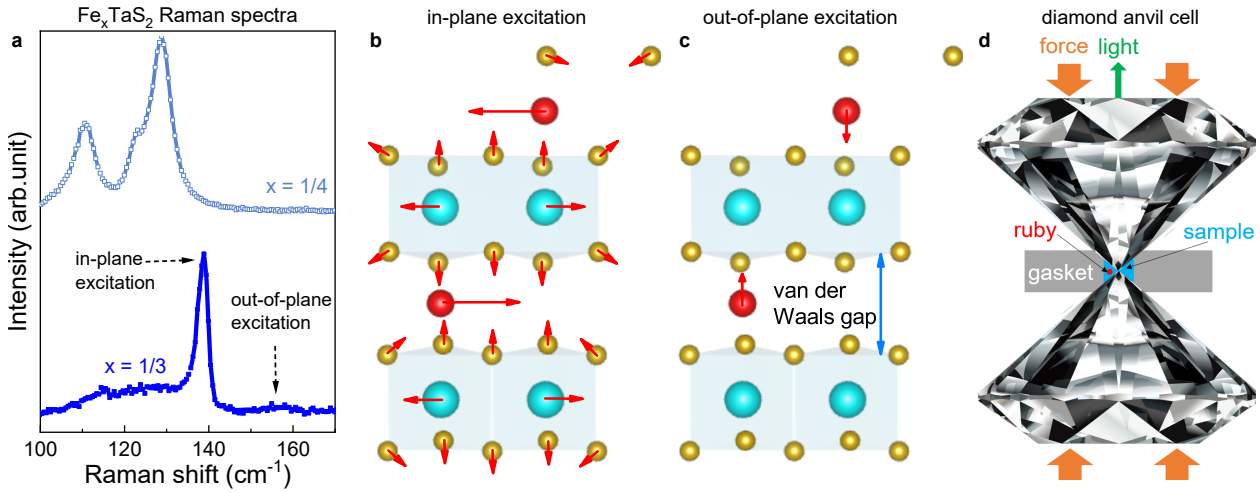

FIG. 1. **Super-lattice excitations in these intercalated chalcogenides.** **a** Close-up view of the intercalated metal monolayer excitations in $Fe_{1/4}TaS_2$ and $Fe_{1/3}TaS_2$. **b,c** Displacement patterns of the in- and out-of-plane metal monolayer excitations for the $x = 1/3$ material obtained from first principles calculations.[49] These excitations emanate from the intercalated metal ions but also involve motion of the sulfur centers in adjacent chalcogenide layers. Additional detail is available in the Supplementary information. **d** Schematic of a diamond anvil cell.

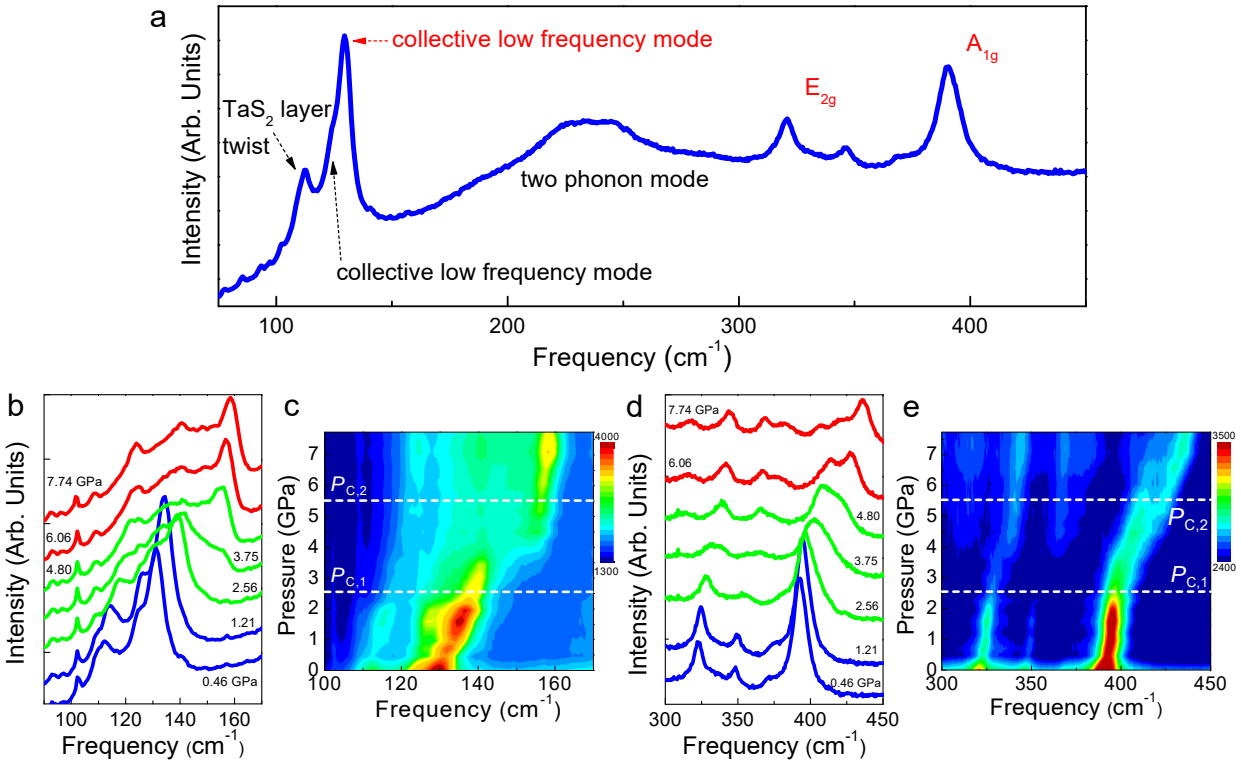

FIG. 2. **Vibrational properties of $Fe_{1/4}TaS_2$ under pressure.** **a** Raman scattering response of $Fe_{1/4}TaS_2$ at ambient conditions along with mode assignments. **b,c** Close-up view of the metal monolayer excitation under compression at 300 K + contour plot showing the location of the critical pressures. **d,e** Close-up view of the chalcogen layer phonons under pressure + contour plot of the same data. The critical pressures are indicated.

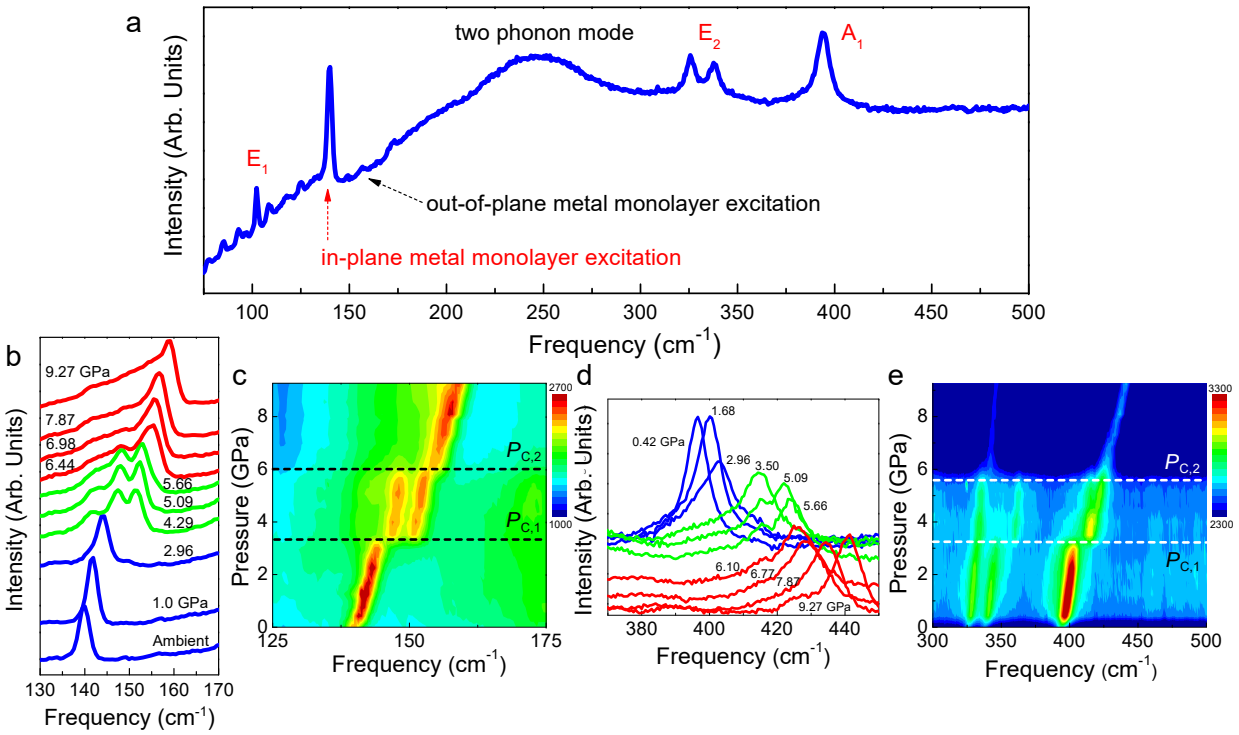

FIG. 3. **Vibrational properties of $Fe_{1/3}TaS_2$ under pressure.** **a** Raman spectrum of $Fe_{1/3}TaS_2$ at ambient conditions along with vibrational mode assignments. **b,c** Close-up view of the metal monolayer mode under compression at 300 K + contour plot of the same data. **d,e** Close-up view of the chalcogen layer phonons under pressure + contour plot of the chalcogen-related phonons. The critical pressures are indicated.

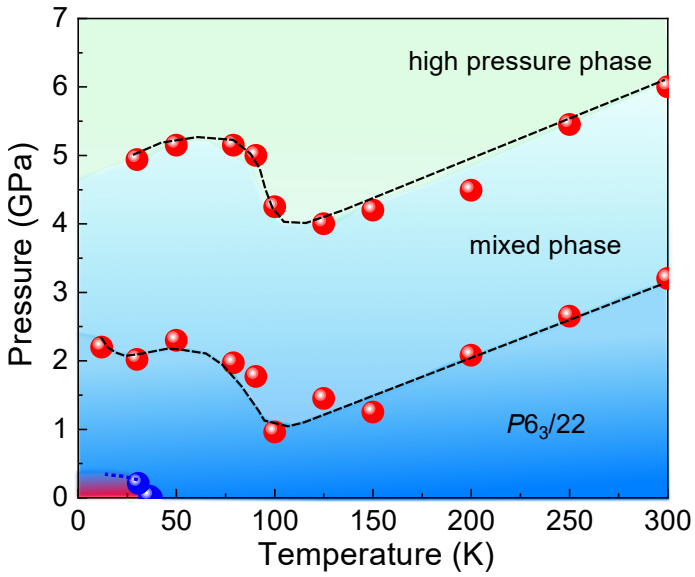

FIG. 4. **P - T phase diagram of the $x = 1/3$ material.** Pressure - temperature phase diagram of $Fe_{1/3}TaS_2$ as revealed by Raman scattering spectroscopy and magnetic susceptibility measurements.

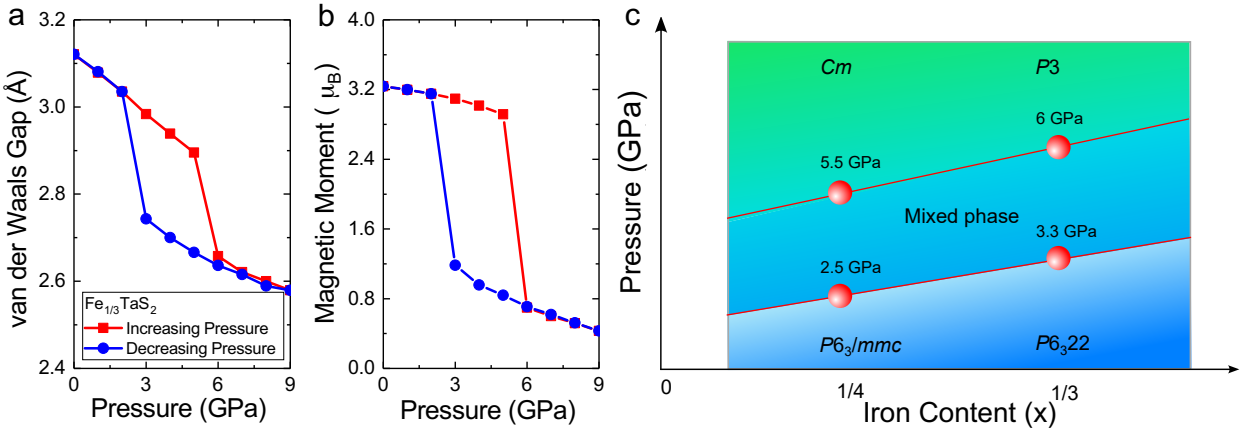

FIG. 5. **van der Waals gap, magnetic moment, and schematic P - x diagram**. **a** Calculated van der Waals gap and **b** magnetic moment on the Fe center as a function of pressure for $Fe_{1/3}TaS_2$. **c** Schematic pressure - composition (P - x) phase diagram for the Fe_xTaS_2 system at room temperature ($x = 1/4$, $1/3$).

TABLES

TABLE I. Summary of the characteristic length scales in this set of intercalated chalcogenides. Charge on the high-spin six-coordinate Fe^{2+} centers is evidenced by unquenched orbital magnetic moment and anisotropy in the $x = 1/4$ material and the fact that saturated moments are the same in both the $x = 1/4$ and $1/3$ compounds.

Material	**Crystal structure at ambient conditions**	A **site ionic radius (Å)**	**Layer thickness (Å)**	**Size of vdW gap (Å)**
$Fe_{1/4}TaS_2$	$P6_3/mmc$, centrosymmetric	0.78	3.104	2.973
$Fe_{1/3}TaS_2$	$P6_322$, chiral + non-centrosymmetric	0.78	3.071	3.071